

HiZELS: a high-redshift survey of H α emitters – I. The cosmic star formation rate and clustering at $z = 2.23$ [★]

J. E. Geach,¹† Ian Smail,¹ P. N. Best,² J. Kurk,³ M. Casali,⁴ R. J. Ivison^{2,5}
and K. Coppin¹

¹*Institute of Computational Cosmology, Durham University, South Road, Durham DH1 3LE*

²*SUPA, Institute for Astronomy, Royal Observatory, University of Edinburgh, Blackford Hill, Edinburgh EH9 3HJ*

³*Max-Planck-Institut für Astronomie, Königstuhl, 17 D-69117, Heidelberg, Germany*

⁴*European Southern Observatory, Karl-Schwarzschild-Strasse 2, D-85738 Garching, Germany*

⁵*Astronomy Technology Centre, Royal Observatory, University of Edinburgh, Blackford Hill, Edinburgh EH9 3HJ*

Accepted 2008 May 17. Received 2008 April 24; in original form 2007 November 30

ABSTRACT

We present results from a near-infrared narrow-band survey of emission-line galaxies at $z = 2.23$, using the Wide Field Camera on the United Kingdom Infrared Telescope. The H₂S1 narrow-band filter ($\lambda_c = 2.121 \mu\text{m}$) we employ selects the H α emission-line redshifted to $z = 2.23$, and is thus suitable for selecting ‘typical’ star-forming galaxies and active galactic nuclei at this epoch. The pilot study was undertaken in the well-studied Cosmological Evolution Survey field (COSMOS) and is already the largest near-infrared narrow-band survey at this depth, with a line flux limit of $F_{\text{H}\alpha} \sim 10^{-16} \text{ erg s}^{-1} \text{ cm}^{-2}$ over 0.60 deg^2 , probing $\sim 220 \times 10^3 \text{ Mpc}^3$ (comoving) down to a limiting star formation rate of $\sim 30 M_{\odot} \text{ yr}^{-1}$ (3σ). In this paper, we present the results from our pilot survey and evaluate the H α luminosity function and estimate the clustering properties of H α emitters at $z = 2.23$ from 55 detected galaxies. The integrated luminosity function is used to estimate the volume-averaged star formation rate at $z = 2.23$: $\rho_{\text{SFR}} = 0.17_{-0.09}^{+0.16} M_{\odot} \text{ yr}^{-1} \text{ Mpc}^{-3}$ for $L_{\text{H}\alpha} > 10^{42} \text{ erg s}^{-1}$. For the first time, we use the H α star formation tracer to reliably constrain ρ_{SFR} out to $z = 2.23$ demonstrating the rapid increase in ρ_{SFR} out to this redshift as well as confirming the flattening in ρ_{SFR} between $z \sim 1$ and 2. In addition to the luminosity distribution, we analyse the clustering properties of these galaxies. Using the two-point angular correlation function, $\omega(\theta)$, we estimate a real-space correlation length of $r_0 = 4.2_{-0.2}^{+0.4} h^{-1} \text{ Mpc}$. In comparison to models of clustering which take into account bias evolution, we estimate that these galaxies are hosted by dark matter haloes of mass $M_{\text{halo}} \sim 10^{12} M_{\odot}$ consistent with the progenitors of the Milky Way.

Key words: galaxies: evolution – galaxies: high-redshift – galaxies: luminosity function, mass function – cosmology: observations.

1 INTRODUCTION

One of the most fundamental, and challenging, goals of modern observational cosmology is to reliably determine the volume-averaged star formation history of the Universe: its distribution function and variation with environment are powerful tools for understanding the physics of galaxy formation and evolution. Surveys using a range of star formation indicators suggest that the star formation rate density (ρ_{SFR}) rises as $\sim(1+z)^4$ out to $z \sim 1$ (e.g. Lilly et al. 1995), and

hence the ‘epoch’ of galaxy formation must occur at $z > 1$. Unfortunately, tying down the precise epoch of maximum activity at $z > 1$ is more difficult, with different star formation indicators giving a wide spread in ρ_{SFR} (e.g. Smail et al. 2002; Hopkins 2004) – although there is a general trend for ρ_{SFR} to plateau at $z \sim 2$ and hence it is likely that many of the stars seen in galaxies at the present-day were formed between $z \sim 1$ and 3. Indeed, $z \sim 2$ –2.5 appears to be a critical era in the evolution of many populations: optical quasi-stellar object (QSO) activity (which should be linked to the growth of super-massive black holes) peaks at this epoch (Boyle et al. 2000), as does the luminosity density in bright submillimetre galaxies – thought to represent an early phase in the formation of massive galaxies (Chapman et al. 2005). This behaviour might be associated with the formation of spheroids or the most massive galaxies. It is

[★]Based on observations obtained with the Wide Field CAMera (WFCAM) on the United Kingdom Infrared Telescope (UKIRT).

†E-mail: j.e.geach@durham.ac.uk

not clear that this evolution is true of ‘typical’ star-forming galaxies (i.e. those with SFRs $< 100 M_{\odot} \text{ yr}^{-1}$). A sensitive survey of star-forming galaxies in a range of representative environments at high z is needed to address this issue.

Variation between the different ρ_{SFR} measurements at high z is in part due to a combination of the effects of sample selection, cosmic variance and biases in individual indicators. Estimates from ultraviolet (UV)-selected samples (e.g. Madau et al. 1996) require large corrections for dust extinction and may miss the most obscured sources altogether. Similarly, although far-infrared-selected samples are less influenced by dust extinction, they require large extrapolations to account for sources below their bright luminosity limits (e.g. Chapman et al. 2005). Thus, while no single indicator can give an unbiased view of the evolution of the ρ_{SFR} , mixing different indicators at different epochs is not helping our understanding.

What we require is one star formation indicator that can be applied from $z = 0$ to 3, is relatively immune to dust extinction and has sufficient sensitivity that ρ_{SFR} estimates do not require large extrapolations for faint sources. The $\text{H}\alpha$ emission-line luminosity is a well-calibrated SFR indicator providing a good measure of the instantaneous SFR of young, massive stars ($> 8 M_{\odot}$; Kennicutt 1998). Thus, $\text{H}\alpha$ combines all of these properties and hence is the tool of choice for studying the evolution of the SFR density out to $z \sim 3$ – covering the expected peak in the ρ_{SFR} . The $\text{H}\alpha$ luminosity function (LF), and the corresponding ρ_{SFR} , has been measured out to $z \sim 1.3$ by a series of investigators (e.g. Gallego et al. 1995; Jones & Bland-Hawthorn 2001; Yan et al. 1999; Tresse et al. 2002; Shioya et al. 2008; Villar et al. 2008). These observations confirm the rapid rise seen by other indicators out to $z \sim 1$ (see also the compilation of Hopkins 2004).

At higher redshift, attempts to search for $\text{H}\alpha$ emission have been made with near-infrared narrow-band surveys (e.g. Thompson, Mannucci & Beckwith 1996; Moorwood et al. 2000), but these have been hampered by small survey areas. At the typical limit of these studies, $F_{\text{H}\alpha} \sim 10^{-16} \text{ erg s}^{-1} \text{ cm}^{-2}$, only a handful of potential $z \sim 2$ $\text{H}\alpha$ emitters have been detected. Indeed, in the largest survey of this type to date, Thompson et al. (1996) detected only *one* $\text{H}\alpha$ emitter over 276 arcmin^2 to a flux limit of $F_{\text{H}\alpha} = 3.5 \times 10^{-16} \text{ erg s}^{-1} \text{ cm}^{-2}$. This was confirmed to have an emission line corresponding to $z = 2.43$ in the follow-up spectroscopic survey of Beckwith et al. (1998). In comparison, Moorwood et al. (2000) probe to a slightly deeper limit, $F_{\text{H}\alpha} = 0.5 \times 10^{-16} \text{ erg s}^{-1} \text{ cm}^{-2}$ over 100 arcmin^2 , and detect 10 candidate emitters, but all of the candidates chosen for spectroscopic follow-up turned out to be higher redshift [O III] $\lambda 5007$ emitters (Moorwood et al. 2003; Kurk et al. 2004). Detecting large numbers of $\text{H}\alpha$ emitters using this method is clearly challenging, and larger (and preferably deeper) surveys are needed to efficiently probe the $\text{H}\alpha$ luminosity density at high redshift.

Larger-scale narrow-band imaging surveys would also present the opportunity to measure the clustering properties of high- z star-forming galaxy populations. Not only does this provide an important insight into the real-space distribution of galaxies, but (assuming a model for bias – i.e. how the observed galaxy populations trace the underlying matter distribution) can also provide an estimate of the mass of dark matter haloes that host such galaxies. Comparing the measurements of clustering for populations at high and low redshift, it is therefore possible to infer the likely progenitor populations of galaxies seen in the local Universe.

In this paper, we make an improvement over previous $z \sim 2$ $\text{H}\alpha$ surveys by utilizing the panoramic imaging capability of the Wide Field Camera (WFCAM; Casali et al. 2007) on the 3.8-m

United Kingdom Infrared Telescope (UKIRT). We have obtained deep narrow-band imaging at $\lambda = 2.121 \mu\text{m}$ to search for $z = 2.23$ $\text{H}\alpha$ emitters over 0.603 deg^2 of the Cosmological Evolution Survey field (COSMOS) (Scoville et al. 2007). This corresponds to a comoving volume ~ 30 times that probed by Moorwood et al. (2000), which is the most similar previous survey in redshift coverage and depth to this one. Here, we present the results of our pilot survey, and use the $\text{H}\alpha$ LF to evaluate the $\text{H}\alpha$ luminosity density at $z = 2.23$, and hence constrain the evolution of ρ_{SFR} . In Section 2, we outline the details of the survey and reduction techniques; in Section 3 we describe the narrow-band selection procedure and in Section 4 we present the results, discuss some of the individual properties and calculate the LF for the $\text{H}\alpha$ sample. We compare our results with previous estimates for this epoch and with the latest semi-analytic predictions for the $\text{H}\alpha$ luminosity density at this epoch. The integrated LF provides us with the ρ_{SFR} , and we compare this to other measurements to place our result in a cosmological context. We also present the first clustering analysis of $\text{H}\alpha$ emitters at high redshift. The two-point angular correlation function yields the real-space correlation length, which we compare to other populations over cosmic time to gain insight into the likely descendants of these galaxies. We summarize the work in Section 5 and give a brief overview of our future extension to the survey. Throughout, we have assumed $h = 0.7$ in units of $100 \text{ km s}^{-1} \text{ Mpc}^{-1}$ and $(\Omega_{\text{m}}, \Omega_{\Lambda}) = (0.3, 0.7)$. Unless otherwise stated, all magnitudes are on the Vega scale.

2 OBSERVATIONS AND DATA REDUCTION

2.1 Observations

The COSMOS field was observed during 2006 May, November and December with WFCAM on UKIRT, with the broad-band (K band) and narrow-band ($\text{H}_2\text{S}1$, $\lambda_c = 2.121 \mu\text{m}$, $\delta\lambda = 0.021 \mu\text{m}$) filters. WFCAM’s standard ‘paw-print’ configuration of four 2048×2048 $0.4 \text{ arcsec pixel}^{-1}$ detectors offset by ~ 20 arcmin can be macro-stepped four times to mosaic a contiguous region of $\sim 55 \times 55$ arcmin (Casali et al. 2007). In this way, we mapped three paw-prints, or $\sim 0.62 \text{ deg}^2$ of COSMOS (centred on $10^{\text{h}}00^{\text{m}}28^{\text{s}}.6$, $+02^{\text{d}}12'21''0$ J2000). Our narrow-band exposure time is $\sim 13.5 \text{ ks pixel}^{-1}$ (in order to reach the equivalent continuum limit, the broad-band K exposures were $\sim 0.5 \text{ ks pixel}^{-1}$). The seeing was consistently of the order of $\lesssim 1$ arcsec. To help with cosmic ray rejection over the relatively long narrow-band exposures (40 or 60 s), we used the Non-Destructive Read (NDR) mode, whereas Correlated Double Sampling (CDS) mode was used for the broad-band exposures. The near-infrared observations were obtained in the standard way, following a 14-point jitter pattern. In addition to the jitter pattern, to improve sampling of the point spread function (PSF) with the 0.4 arcsec pixel of WFCAM, the narrow-band frames were microstepped in a 2×2 grid with 1.2 arcsec offsets at each position. We summarize the observations in Table 1.

2.2 WFCAM data reduction

For a given frame in a jitter sequence of 14 images, we self-flat the data using a normalized median combination of the remaining frames in the sequence, taking care to mask-out bright objects in each frame. This is achieved by creating a two-pass flat: in the first pass, a rough flat-field image is made from a straight median combination of the data frames in order to reveal the bright objects. In the next step, we use SEXTRACTOR’S CHECK_IMAGE output (v2.3.2; Bertin

Table 1. Observation log of the COSMOS field. Coordinates are in J2000 and refer to the centre pointing of a WFCAM ‘paw-print’. The average seeing in the broad- and narrow-band frames (stacked frames) is ~ 1 arcsec.

| Field ID | RA (h m s) | Dec. ($^{\circ}$ ' ") | Dates observed | H $_2$ S1 exposure time (ks) | Continuum (K) depth (3σ mag) |
|----------|---------------|---------------------------|---------------------------------------|---------------------------------|---------------------------------------------|
| COSMOS 2 | 10 00 52 | +02 10 30 | 2006 May 20–26/2006 December 5, 14–20 | 15.9 | 20.1 |
| COSMOS 3 | 10 00 00 | +02 23 44 | 2006 May 20–26/2006 December 5, 14–20 | 13.4 | 20.0 |
| COSMOS 4 | 10 00 53 | +02 23 44 | 2006 November 13–17 | 13.6 | 20.1 |

& Arnouts 1996) to identify regions where bright stars and galaxies lie and then mask these when constructing the master flat. This minimizes the artefacts seen around bright sources. Some care must be taken with the micro-stepped frames – the small offset between consecutive frames in a micro-sequence is smaller than many extended sources, therefore we construct flats for each position in the micro-stepped sequence separately as if they are part of a standard dither.

A world coordinate system is fit to each frame by querying the United States Naval Observatory A2.0 catalogue, fitting on average ~ 100 objects, and then frames are aligned and co-added with SWARP¹ (this performs a background mesh-based sky subtraction, optimised to provide the best representation of the large-scale variations across the field). In the case of the micro-stepped (narrow-band images), this step is preceded by drizzling the frame on to a grid with a pixel scale of 0.2 arcsec (i.e. half the camera pixel scale).

WFCAM frames suffer from significant cross-talk, manifesting itself in toroidal features at regular (integer multiples of 128) pixel intervals from sources in the read-out direction. As these are tied to the positions of real objects, they are not removed by dithering the frames. High-order cross-talk can easily mimic real objects, therefore these positions are flagged at the catalogue stage; we discuss this further in Section 3.

Broad-band and narrow-band frames are calibrated by matching $10 < K < 15$ stars from the Two-Micron All-Sky Survey (2MASS) All-Sky Catalogue of Point Sources (Cutri et al. 2003) which are unsaturated in our frames. Since the narrow-band filter falls in the K band, we can check the zero-point offsets to be applied to the narrow-band frames directly from the broad-band calibration, taking into account the relative widths of the filters, such that the offset between the zero-points is $2.5 \log(\Delta\lambda_K / \Delta\lambda_{H_2S1})$. As an additional verification, we check that $K - H_2S1 \sim 0$ as expected using the photometry of the bright stars. We estimate our absolute K calibration is good to $\lesssim 1$ per cent from the scatter compared to 2MASS.²

2.3 Source extraction and survey limits

Our survey is made up of a mosaic of three WFCAM paw-prints, i.e. twelve 13.7×13.7 arcmin² tiles. Sources are detected and extracted using SExtractor (Bertin & Arnouts 1996). A final narrow-band catalogue is made by matching detections in the H $_2$ S1 to the broad-band image. Since the frames are astrometrically well aligned, a simple geometric matching algorithm suffices, with a maximum search radius of 2 arcsec. Cross-talk artefacts in WFCAM frames

can mimic the narrow-band excess objects we are selecting for. Therefore, to clean the catalogue from possible cross-talk contaminants we measure the chip (x, y) position of bright sources, and flag regions at integer multiples of 128 pixels along the direction of readout. These chip positions can be converted to a sky coordinate and then compared to the narrow-band catalogue. As a rule, we remove an object from the catalogue if it lies within 2 arcsec of any cross-talk position. Note that by avoiding the zeroth-order cross-talk position, we also avoid spurious detections close to bright stars (although in this case the exclusion radius is larger to account for extended haloes and diffraction spikes, at 30 arcsec). Due to the lower exposures received by the edges of the individual frames (caused by the jitter pattern), we ignore detections from within ~ 10 arcsec of any frame edge. The total area lost due to cross-talk and star masking is negligible (< 0.1 per cent), however including the edge-clipping we survey an effective area of 0.603 deg².

Due to the fact that the observations were acquired over a long period of time, with slightly different seeing and exposure times (Table 1), we treat each tile separately, detecting objects down to each tile’s limit. The average 3σ depth of the broad-band frames is $K = 20.1$ mag. We detect a total of 19 079 objects down to this limit across 0.603 deg². Note that all magnitudes are measured in 3 arcsec diameter apertures, and this recovers the majority of the flux.

To confirm the depth and completeness of the images, we perform Monte Carlo simulations of the detection of a large number of ‘fake’ sources (a single Gaussian point source generated with IRAF’s ARTDATA with a full width at half-maximum (FWHM) matching the image PSF). By scaling the artificial source over a range of known flux, and inserting at random locations over the frames, we measure the detection rate (i.e. the completeness) as a function of observed magnitude using an identical extraction procedure to that used to generate the main catalogue. We use this detection completeness information to correct the derived LF of H α emitters.

3 SELECTION TECHNIQUE

3.1 Narrow-band excess selection

Potential $z = 2.23$ H α emitting candidates are initially selected based on the significance of their narrow-band excess, i.e. their $K - H_2S1$ colour. Galaxies with a strong emission line falling in the narrow-band filter will have $H_2S1 < K$. The significance of the narrow-band excess can be parametrized in terms of Σ , which quantifies the excess compared to what would be expected for a source with a flat spectrum (Bunker et al. 1995). This parameter is similar to a standard signal-to-noise ratio (S/N) selection, and we chose to select candidate emitters with $\Sigma > 2.5$. This is equivalent to a colour of

$$m_K - m_{H_2S1} = -2.5 \log [1 - \Sigma \delta 10^{-0.4(c - m_{H_2S1})}], \quad (1)$$

¹ Both SWARP and SExtractor are distributed by Terapix (<http://terapix.iap.fr>) at the Institut d’Astrophysique de Paris.

² An independent data reduction of a sub-set of the science frames by the Cambridge Astronomical Survey Unit (CASU) confirms consistent photometry (M. Riello, private communication).

where c is the zero-point of the narrow-band image and δ is the photometric uncertainty. The $H\alpha$ line flux $F_{H\alpha}$ and equivalent width $W_{H\alpha}$ can be calculated as

$$F_{H\alpha} = \Delta\lambda_{H_2S1} \frac{f_{H_2S1} - f_K}{1 - (\Delta\lambda_{H_2S1}/\Delta\lambda_K)} \quad (2)$$

and

$$W_{H\alpha} = \Delta\lambda_{H_2S1} \frac{f_{H_2S1} - f_K}{f_K - f_{H_2S1}(\Delta\lambda_{H_2S1}/\Delta\lambda_K)} \quad (3)$$

where $\Delta\lambda_K$, $\Delta\lambda_{H_2S1}$ are the widths of the broad- and narrow-band filters and f_K and f_{H_2S1} are the flux densities in the two filters. $W_{H\alpha}$ is simply the ratio of the line flux and continuum flux density, and will also include contribution from the adjacent $[N\text{ II}]$ line. However, we calculate the expected $H\alpha$ line flux by assuming $F_{[N\text{ II}]} / F_{H\alpha} = 0.33$ for extragalactic $H\text{ II}$ regions (Kennicutt & Kent 1983) and correcting appropriately. Note that this may result in conservative $H\alpha$ fluxes, since for metal-poor galaxies this contribution may be lower.

In Fig. 1, we present the colour–magnitude diagram with selection criteria. Some care must be taken in deciding on the selection, and we briefly describe it here. First, we only use narrow-band detections with detection significances of $>3\sigma$. It is not necessary that the source is also detected in the broad-band frame, and we assign an upper limit if there is no corresponding continuum detection. We define initial selection criteria of $\Sigma > 2.5$ (this is a function of narrow-band flux and combined error due to sky noise in both the broad- and narrow-band images, as described above.). We account for bright foreground objects with steep continua across the K band by making use of the $z - K$ colours available for all detections from the COSMOS archival z -band imaging (Capak et al. 2007).

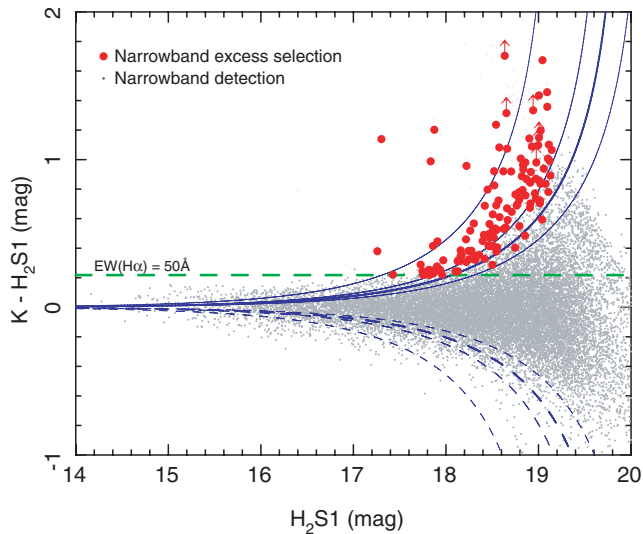


Figure 1. The $K - H_2S1$ colour–magnitude diagram used to select narrow-band excess objects, and thus possible $z = 2.23$ $H\alpha$ emitters. Narrow-band colours have been corrected to account for broad-band continuum slope using the $(z - K)$ broad-band colour (see Section 3.1). $\Sigma = 2, 2.5, 3$ and 5 selection cuts are shown, as is a 50 \AA minimum in equivalent width used to select significant emitters. The Σ cuts here are averaged over the whole field area, but these change slightly for each WFCAM tile as we take into account individual frame zero-points and noise properties (although there is only a small variation over the survey). We show all detections that would have been selected as narrow-band excess sources as filled circles (limits indicate that source was not detected in the broad-band frame). These narrow-band excess sources are subject to a further selection described in more detail in Section 3.2.

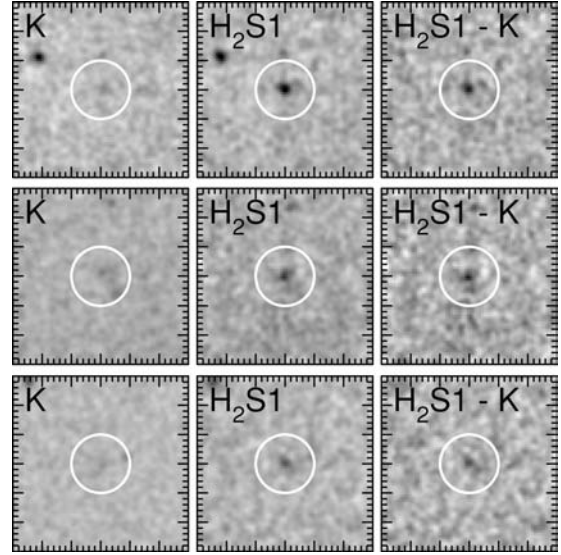


Figure 2. Three examples of narrow-band excess sources of various significance, Σ . The top, middle and lower panels show $\Sigma \sim 5$, $\Sigma \sim 3$, $\Sigma \sim 2.5$, respectively. The left-hand panels show the K -band continuum, the centre shows the H_2S1 narrow-band image and the right-hand panel shows the continuum-subtracted narrow-band image. The K -band image has been scaled to account for the filter widths and both frames were locally registered with improved astrometric accuracy and smoothed with a Gaussian kernel to the same effective seeing. Images are $30 \times 30 \text{ arcsec}^2$ and are orientated as north up and east towards left and scaled identically. Note that all images have been rebinned to the scale of the K -band frame: $0.4 \text{ arcsec pixel}^{-1}$.

Their very red continua will result in a larger effective wavelength for the broad-band detections. We correct for this to make a better estimate of the continuum contribution to the narrow-band flux at the $2.121 \mu\text{m}$. We measure $K - H_2S1$ as a function of $(z - K)$, and fit the data with a linear trend using a least-squares fit. The slope of this line is then used to correct the $K - H_2S1$ colour. We find that on average the correction factor to the narrow-band magnitude excess is $0.03(z - K)$. To account for narrow-band detections that have large significance but low equivalent widths (e.g. van der Werf, Moorwood & Bremer 2000), we enforce additional selection criteria of $W_{H\alpha} > 50 \text{ \AA}$. This is an arbitrary threshold, but is chosen to reflect the general scatter about $K - H_2S1 = 0$ (see Fig. 1).

The $H\alpha$ line-flux limit is the theoretical minimum that could be detected taking into account all these selection criteria. The average 3σ $H\alpha$ flux limit over the survey is $1 \times 10^{-16} \text{ erg s}^{-1} \text{ cm}^{-2}$. As a final quality-control check, we visually inspect each candidate in order to filter any remaining erroneous sources (e.g. non-cross-talk associated artefacts, etc.). In Fig. 2, we present the narrow-band field around three candidate emitters representing a range of detection significance ($2.5 \lesssim \Sigma \lesssim 5$). For each panel, we show the narrow-band frame before and after continuum subtraction using the broad-band image after suitably scaling to account for the relative filter widths. We detect a total of 180 sources meeting the narrow-band selection criteria across 0.603 deg^2 .

3.2 Broad-band colours: further selection, redshift confirmation and line contamination estimates

We must be certain that the selection in colour space is actually identifying the $H\alpha$ line at $z = 2.23$ rather than another strong emission line at another redshift. At higher redshift, the most important

contaminant is [O III] λ 5007 at $z = 3.23$ (although these objects are interesting in their own right as possible examples of high- z active galactic nuclei (AGN) or star-forming galaxies). At low redshift, we are potentially susceptible to any strong line with an emission wavelength between H α and H $_2$ S1.

The most robust way to confirm the selection is through follow-up spectroscopy which can unambiguously identify the lines. However, complete spectroscopic follow up (at least in the short term) is unfeasible. A ‘cheaper’ alternative is to make use of extensive multi-band optical/near-infrared photometry available for COSMOS (Capak et al. 2007), which can be used to improve the H α selection. Unfortunately, at $z = 2.23$ the current photometric redshifts are not reliable enough to confirm H α emission (Mobasher et al. 2007), so we turn to the cruder method of colour/colour-selection to clean our high-redshift sample.

We therefore define a secondary optical selection, tuned according to the colours of a sub-sample of high-significance ($\Sigma > 5$) H α candidates from the pure narrow-band selection. To discriminate between high- and low-redshift emission-line galaxies, we first use the *sBzK* selection first presented by Daddi et al. (2004), and now becoming popular to select active galaxies at $z > 1.4$. An alternative selection of high-redshift galaxies is made with *ugr* colours, and has been used to search for $z \sim 3$ Lyman Break galaxies (LBGs; Steidel et al. 1996) and ‘BM/BX’ star-forming galaxies at $z \sim 2$ (Steidel et al. 2003; Adelberger et al. 2004). We use the BM/BX selection as a further indicator that the narrow-band-selected galaxies are at a high redshift (additionally the LBG selection can also be used to detect possible $z \sim 3$ [O III] λ 5007 emitters). Candidate H α emitters are narrow-band excess objects which also satisfy the BM/BX selection *or* the *sBzK* selection. In a further effort to eliminate foreground contaminants, we impose a magnitude cut of $z < 22.5$ (equivalent to $M_u < -23.7$ at $z = 2.23$). This yields a total H α sample of 55 compared to our original selection of 180 sources on the basis of narrow-band selection alone. We present the colour–colour plots with selection criteria in Fig. 3. After the colour selection, the majority of H α emitters fall in both the BM/BX

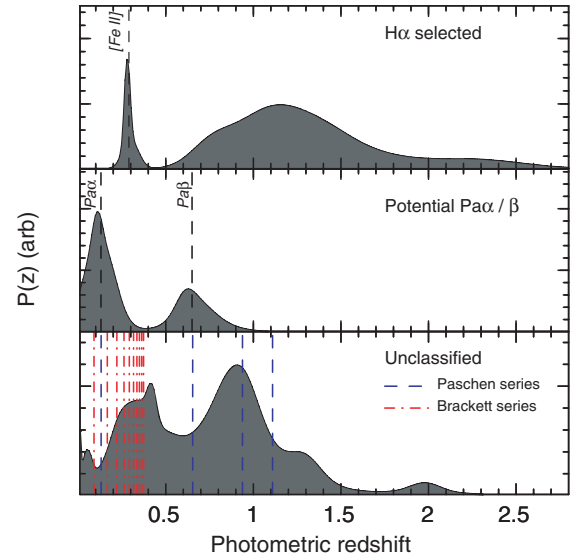


Figure 4. The summed probability distributions $P(z)$ for photometric redshifts: (top) narrow-band excess detections satisfying our *ugr/BzK* selection. Note that there is a spike in $P(z)$ at $z \sim 0.3$, corresponding to the redshift of [Fe II] λ 1.64 in the H $_2$ S1 filter. This spike represents two objects and these are removed from our sample. The broad distribution of z_{phot} at $z \gtrsim 1$ is probably real H α emitters with poorly determined photometric redshifts; (middle) distribution of galaxies selected as Pa α and Pa β emission lines with $z_{\text{phot}} = 0.13 \pm 0.05$ and 0.65 ± 0.05 , respectively; (bottom) remaining ‘unclassified’ emitters. There are two main peaks to the distribution of unclassified objects: at $z \sim 0.3$ which could correspond to [Fe II] λ 1.64 or several Brackett lines. At $z \sim 0.8$, the peak could correspond to Pa γ .

and *sBzK* regions, with those that do not have large enough photometric errors that place them $< 1\sigma$ away in colour space. Note that two objects flagged as H α emitters are potentially low-redshift [Fe II] λ 1.64 emitters based on their photometric redshifts (see Fig. 4 and discussion below). Thus, the photometric selection is not a

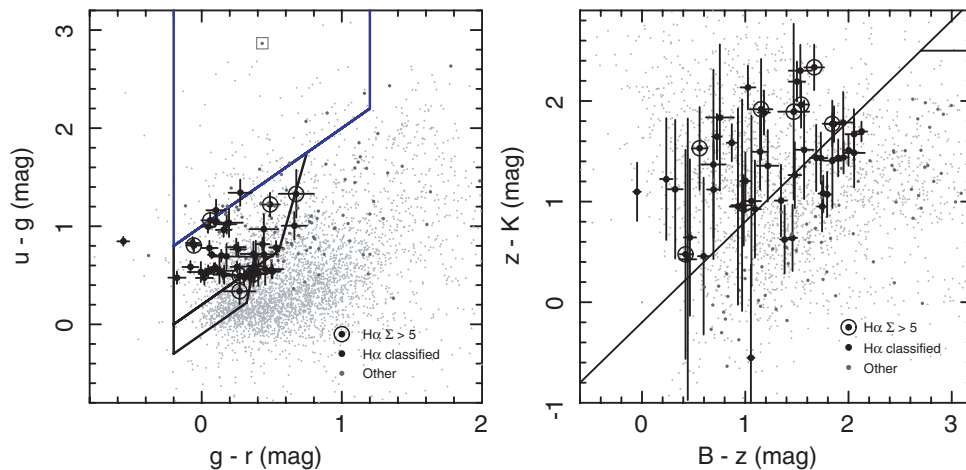


Figure 3. Broad-band colours of narrow-band-selected objects from our survey. Left-hand panel: *ugr* colours with the LBG and BM/BX selection criteria of Steidel et al. (2003); right-hand panel: *BzK* colours divided into high-redshift star-forming galaxies (*sBzK*) and high-redshift passive galaxies (*pBzK*) and foreground galaxies, using the selection of Daddi et al. (2004). In both cases, we compare to a 1-in-100 sampling of the general colour distribution using photometry available for the COSMOS field. It is clear that the straightforward narrow-band selection outlined in Section 3.1 is also detecting low-redshift galaxies, and we require further selection with broad-band colours to identify these. However, the low-redshift detections likely correspond to *real* emission lines, and we discuss this further in Section 3.2. Large points indicate our secure H α emitters after employing our secondary colour selection outlined in Section 3.2 and we highlight the high-significance ($\Sigma > 5$) candidates, noting that all of these fall in the *sBzK* and BX/BM selection regions. For clarity, we only show photometric uncertainties for H α candidates.

foolproof method, although it suggests the contamination rate is low ($\lesssim 3$ per cent). To estimate the number of galaxies that could have been potentially missed by this further colour selection, we Monte Carlo our selection by allowing the photometry to vary randomly in a range defined by the (1σ) uncertainty on each point, then count the number of galaxies satisfying the $H\alpha$ criteria and compare this to the nominal value. Repeating this procedure many times builds up a measure of the likely contamination/incompleteness as galaxies are scattered in and out of the selection regions. Our results suggest that the number of galaxies missed (or alternatively the interloper fraction) could be as much as 10 per cent. Assessing this contamination more accurately will require follow-up spectroscopy, which, at the time of writing, is underway.

What are the remaining narrow-band excess objects which fail our colour selection? At least one appears to be a high-redshift (possibly $[O\text{III}]\lambda 5007$) emitter selected in the LBG cut, but the bulk of the remaining objects are likely to be low redshift given their colours. There are several other low-redshift emission lines that could potentially be detected, and to investigate this, in Fig. 4, we plot the probability distribution $P(z)$ of z_{phot} of (i) candidate $H\alpha$ emitters, (ii) $Pa\alpha$ and $Pa\beta$ candidates and (iii) unclassified remaining narrow-band excess detections. Using a conservative photometric redshift uncertainty of $dz = \pm 0.05$, we identify 12 $Pa\alpha$ and six $Pa\beta$ candidates. In the unclassified redshift distribution, there are two clear peaks in the distribution at $z \sim 0.4$ and ~ 0.9 . The low-redshift emitters could potentially be $[\text{Fe}\text{II}]\lambda 1.6\ \mu\text{m}$ or several Brackett lines, whereas the slightly higher redshift peak might correspond to $Pa\gamma$. Clearly, this must be confirmed through spectroscopy, but it appears that the narrow-band selection is detecting real line-emitters, but is not sufficient alone to isolate $H\alpha$ at $z = 2.23$. The identification of lower redshift interlopers will become easier when more accurate photometric redshifts are available for COSMOS (Mobasher et al. 2007; Mobasher, private communication).

To check for contamination for higher- z line emitters, we use a ugr cut to select $z \sim 3$ LBGs, and so identify possible $[O\text{III}]\lambda 5007$ contaminants (Fig. 3). In our total narrow-band-selected sample, only one object satisfies the LBG selection criteria, and therefore we conclude that the $z = 3.23$ $[O\text{III}]\lambda 5007$ contamination rate is negligible for our sample. We note that in a follow up, spectroscopic survey of narrow-band identified $z = 2.2H\alpha$ emitters by Moorwood et al. (2000), six of 10 candidates were confirmed as $z = 3.23$ $[O\text{III}]\lambda 5007$. Thus, it is not clear whether environmental effects are responsible for the high contamination observed in this previous small-scale survey.

Finally, we assess the impact of contamination from AGN at $z = 2.23$ which would impact on our assessment of ρ_{SFR} from the $H\alpha$ LF. We are probing the expected peak in the SFRD, but this is also associated with the peak of AGN activity (Shaver et al. 1996; Boyle & Terlevich 1998) – what is the expected contamination rate in our $H\alpha$ -selected sample? As with contamination from emission lines at different redshifts, without spectroscopic information (e.g. the $H\alpha/[\text{N}\text{II}]$ ratio discriminating between star formation and nuclear activity), we must address this issue statistically. As described by van der Werf et al. (2000), the AGN interloper fraction is likely to be low: the fraction of AGN in local $H\alpha$ -selected galaxies is < 5 per cent (Gallego et al. 1995), and this is not likely to increase toward high redshift (Teplitz, Malkan & McLean 1998). On the other hand, Shioya et al. (2008) include a 15 per cent correction for AGN contamination in the $H\alpha$ LF at $z = 0.24$, based on the results of Hao et al. (2005) who studied the $H\alpha$ luminosity density from AGN in the Sloan Digital Sky Survey. We adopt this same

15 per cent AGN contamination in our measurement, resulting in a more conservative estimate of ρ_{SFR} .

3.3 Spectroscopic comparison

The z COSMOS survey (Lilly et al. 2007) is an extensive spectroscopic project obtaining thousands of redshifts in the COSMOS field. To search for any existing spectra corresponding to our narrow-band excess sample, we cross-correlate our catalogue with the current z COSMOS spectroscopic catalogue (S. Lilly, private communication). We do not expect a large degree of overlap between our catalogue and z COSMOS, since we are detecting relatively faint galaxies, and indeed there were only five matches with secure redshifts. One $H\alpha$ candidate is included in the ‘faint’ z COSMOS catalogue and confirmed to securely lie at $z = 2.2329$, verifying the selection at least for this candidate. The remaining matches are all in the ‘bright’ sample. Three of these were identified by us as being possible $Pa\alpha$ at $z \sim 0.13$, and indeed two have confirmed redshifts of $z = 0.1312$ and 0.1298 , although another has $z = 0.1086$. The final match has $z = 0.7340$, and it is unclear if this corresponds to a real emission line. Although this is a very limited spectroscopic confirmation, it does suggest that we are detecting a range of emission lines, and that our secondary filtering technique is useful for weeding out low-redshift interlopers. We note that our near-infrared spectroscopic follow-up will allow us to make a much better estimation of the contamination rate.

4 RESULTS

We detect a total of 55 robust candidate $z = 2.23$ $H\alpha$ emitters over $0.603\ \text{deg}^2$ of the COSMOS field, resulting in a surface density of $91 \pm 10\ \text{deg}^{-2}$ above a flux limit of $1 \times 10^{-16}\ \text{erg s}^{-1}$, equivalent to a SFR of $30 M_{\odot}\ \text{yr}^{-1}$ at this redshift. In the following sections, we briefly discuss their multi-wavelength and morphological properties, and use the sample to evaluate the $H\alpha$ LF and thus star formation rate density at $z = 2.23$. Finally, we make an estimate of the real-space correlation length of $H\alpha$ emitters by measuring their two-point angular correlation function.

4.1 $H\alpha$ luminosity density at $z = 2.23$

4.1.1 Evaluating the LF of $H\alpha$ emitters

To calculate the LF of $H\alpha$ emitters, we convert line fluxes to luminosities, correcting for 33 per cent $[\text{N}\text{II}]$ contribution to the measured flux. The volume is reasonably well defined by the survey area and narrow-band filter width (50 per cent cut-on/off: $2.111\text{--}2.132\ \mu\text{m}$), which probes a comoving depth of $\sim 40\ \text{Mpc}$, and is equivalent to $220 \times 10^3\ \text{Mpc}^3$ (comoving). However, the reader should note that since the narrow-band transmission function is not a perfect top-hat, the effective volume probed will vary as a function of intrinsic luminosity, with more luminous $H\alpha$ emitters being detected over a larger volume than fainter sources. Similarly, the incompleteness will vary strongly as a function of apparent luminosity, since faint $H\alpha$ emitters at redshifts corresponding to the low-transmission wings of the narrow-band filter might be lost, and bright lines will have their luminosity underestimated, contributing to the counts in lower luminosity bins. To estimate the impact of this effect on our measured results, we model these observational effects on a ‘true’ model LF. Our simulation consists of a set of

model H α emission lines convolved with the H₂S1 transmission function, where the lines are randomly placed in a redshift range corresponding to the full width of the filter. After convolving 1000 such lines per luminosity interval, we recover the effective volume probed, the incompleteness and luminosity biases (i.e. including intrinsically bright emitters dimmed by the edge of the transmission function falling in lower luminosity bins). The combination of these effects modifies the model LF, the main change being an ~ 10 per cent reduction in the faint-end slope α and an ~ 20 per cent decrease in ϕ^* compared to a uniform transmission model. The effect on L^* is negligible. As we describe below, since we fix the faint-end slope $\alpha = -1.35$, the difference in the integrated LF above the simulated detection threshold is slightly less than if this was a free parameter, ~ 10 per cent, and we correct for this difference in our measurement of ρ_{SFR} .

Although H α is relatively insensitive to dust extinction (unlike Ly α , it is not resonantly scattered), dust absorption must still be taken into consideration when deriving luminosities. A robust technique would be to obtain spectroscopy of each source to measure the Balmer H α /H β decrement, but this is not currently feasible for our sample. Instead, we simply adopt $A_{\text{H}\alpha} = 1$ mag (Kennicutt 1992, 1998), as is applied in similar earlier studies (Fujita et al. 2003; Pascual et al. 2005; Ly et al. 2007) for SFR estimates. Although it is known that the specific extinction is a function of SFR (Hopkins et al. 2001; Jansen, Franx & Fabricant 2001; Aragón-Salamanca et al. 2003), for ease of comparison with other samples, we apply this constant correction to our sample, noting that in the cases where the actual extinction is higher, our measured SFRs will be conservative. We compare SFR indicators for our sources in Section 4.2.2 and confirm that the correction used here is appropriate.

Our LF has been corrected for completeness on a bin-by-bin basis using the completeness functions estimated from the narrow-band simulation (Section 2.3), and the lower luminosity limits have been dealt with by performing a survival analysis on the binned data, using the probability estimator of Avni et al. (1980). Note that we apply a correction for the incompleteness caused by the shape of the H₂S1 transmission described above on the integrated LF (see Section 4.1.2). The errors are derived from the Poisson statistics of each bin, although we apply a slightly more conservative bootstrap analysis to estimate the uncertainties on the fit values, described in more detail below. We fit the LF with a Schechter function characterized by α , ϕ^* and L^* : $\phi(L)dL = \phi^*(L/L^*)^\alpha \exp(-L/L^*)d(L/L^*)$. Since we lack sufficient depth to fit the faint-end slope, we fix $\alpha = -1.35$, the value observed by Gallego et al. (1995) for their $z = 0$ H α study. This approach was also used by Yan et al. (1999) for the H α LF at $z = 1.3$. Therefore, we cannot show any evolution in the faint-end slope of the H α LF – a deeper survey is required for this. In fact, Reddy et al. (2008) find evidence for a steeper faint-end slope for UV/optical colour-selected star-forming galaxies at high redshifts ($z \sim 2-3$). Adopting a $\alpha < -1.35$ would obviously have a rather dramatic effect on extrapolated values for ρ_{SFR} , which we discuss in Section 4.1.2.

To estimate uncertainties on the LF, we refit the Schechter function by bootstrapping, with the variance of the resulting parameters forming our uncertainty in ϕ^* and L^* . We find $\phi^* = (1.45 \pm 0.47) \times 10^{-3} \text{ Mpc}^{-3}$ and $\log L^* = 42.83 \pm 0.13 \text{ erg s}^{-1}$. We present the results in Fig. 5 in comparison to lower redshift studies of the H α LF $z = 0$, demonstrating the sharp increase in H α emitters from $z = 0$ to 2.23. Our results are very similar to the luminosity distribution found by Yan et al. (1999), suggesting that there is little evolution of the bright end of the H α LF across the 2 Gyr between $z = 2.23$ and 1.3.

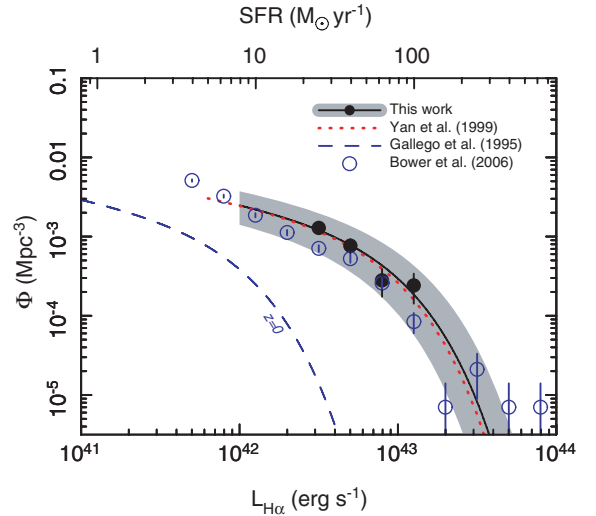


Figure 5. H α LF from this work compared to those derived at $z = 0$ (Gallego et al. 1995) and $z = 1.3$ (Yan et al. 1999). Note that the observational LFs in this figure have not been corrected for dust extinction. Errors are based on the Poisson counting error and the completeness correction applied to each bin, derived from the detection rate of narrow-band-selected sources. The LF is fit with a Schechter function with a fixed faint-end slope, $\alpha = -1.35$ (identical to Yan et al. 1999; Gallego et al. 1995) – deeper observations will be required to probe the evolution of the faint-end slope of the LF. Our results show significant evolution from $z = 0$ equivalent to an order of magnitude in luminosity evolution. Our LF is also very similar to the $z = 1.3$ H α LF, with little or no evolution between $z = 2.23$ and 1.3, interpreted in terms of the star formation rate density as a peak or plateau occurring at $z \sim 2$ (see Fig. 6). We compare to the theoretical prediction of the luminosity distribution of H α emitters from the B06 variant of the semi-analytic GALFORM code (Cole et al. 2000). The observed counts agree well with the model, although there are hints that the faint-end slope is slightly steeper than our assumed value.

4.1.2 The star formation rate density at $z = 2.23$

Next, we use the integral of the LF to find the volume-averaged star formation rate density, ρ_{SFR} . In Fig. 6, we present the evolution of ρ_{SFR} out to $z = 2.23$ using H α only. In order to compare results, we take the LF parameters for H α surveys compiled by Hopkins (2004) and integrate these down to $L_{\text{H}\alpha} = 10^{42} \text{ erg s}^{-1}$, the approximate luminosity limit of the present survey. To convert H α luminosity to a star formation rate, after applying a factor of 2.5 to $L_{\text{H}\alpha}$ to account for $A_{\text{H}\alpha} = 1$ mag, we use the standard calibration of Kennicutt (1998); $\text{SFR}[\text{H}\alpha] = 7.9 \times 10^{-42} (L_{\text{H}\alpha}/\text{erg s}^{-1}) \text{ M}_{\odot} \text{ yr}^{-1}$ [assuming continuous star formation, Case B recombination at $T_e = 10^4 \text{ K}$ and a Salpeter initial mass function (IMF) ranging from 0.1 to 100 M_{\odot}]. Correcting for the transmission incompleteness described in Section 4.1.1 and a 15 per cent correction for AGN contamination (Shioya et al. 2008), we find $\rho_{\text{SFR}} = 0.17^{+0.16}_{-0.09} \text{ M}_{\odot} \text{ yr}^{-1} \text{ Mpc}^{-3}$ where the uncertainty is equivalent to the 1σ uncertainties on the LF fit parameters. Our results support a flattening or peak in the level of star formation activity between $z \sim 1$ and 2.

In Fig. 6, we also show the evolution of ρ_{SFR} , but extrapolated to a much fainter luminosity, $L_{\text{H}\alpha} > 10^{37} \text{ erg s}^{-1}$ ($\text{SFR} > 8 \times 10^{-5} \text{ M}_{\odot} \text{ yr}^{-1}$), in line with the ρ_{SFR} compilation of Hopkins (2004). We remind the reader of the uncertainty inherent in interpreting ρ_{SFR} estimates derived from such extrapolations: the uncertainty in the slope of the faint end of the LF could have a dramatic effect on the result. For this extrapolated case (again, corrected for extinction), we find $\rho_{\text{SFR}} = 0.25^{+0.20}_{-0.13} \text{ M}_{\odot} \text{ yr}^{-1} \text{ Mpc}^{-3}$.

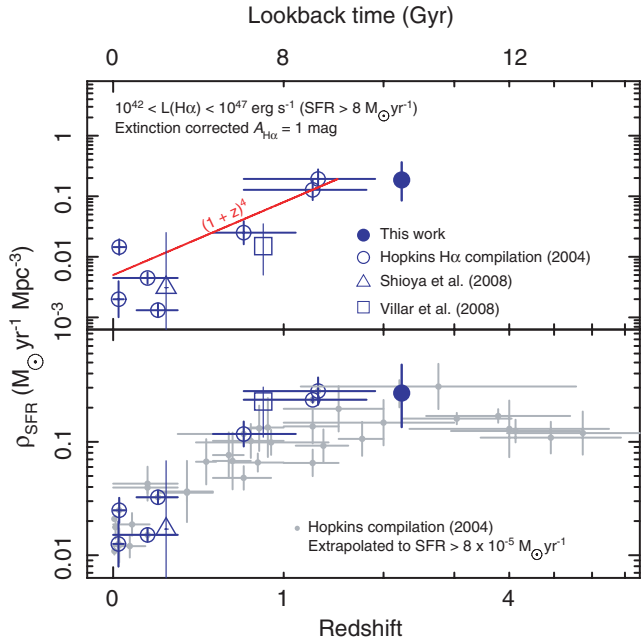


Figure 6. The evolution of the star formation rate density out to $z = 2.23$ using the $H\alpha$ tracer alone, and compared to a heterogeneous mix of multi-wavelength tracers (all converted to the cosmological parameters used throughout this work). The data are collected from the compilation of literature data made by Hopkins (2004), and recent works of Shioya et al. (2008) and Villar et al. (2008). Where corrected for extinction, data are modified by a common factor $A_{H\alpha} = 1$ mag. In the top panel, we calculate the integrated $H\alpha$ luminosity down to the approximate luminosity limit of the present survey, $L_{H\alpha} > 10^{42}$ erg s $^{-1}$. Our results support a flattening of the ρ_{SFR} between $z \sim 1$ and 2. In the bottom panel, we apply the same integration range as Hopkins (2004), extrapolating down to $L_{H\alpha} > 10^{37}$ erg s $^{-1}$. The general evolution of ρ_{SFR} is mirrored here, but the reader should be aware of the potentially strong impact uncertainties in the faint-end slope have on the integrated LF. Surveys of high-redshift star-forming galaxies have yet to satisfactorily constrain this parameter.

This is in broad agreement with the range of ρ_{SFR} estimates (for a variety of tracers) at $z = 2.23$ (Fig. 6) and confirms the plateau in ρ_{SFR} above $z \sim 1$.

Our measurements of ρ_{SFR} are consistent with the results of Reddy et al. (2008), who estimate the $H\alpha$ luminosity density at $1.9 \leq z < 2.7$ by using the correlation between dust-corrected UV and $H\alpha$ SFRs (Erb et al. 2006). They find $\rho_{SFR} = 0.35 \pm 0.09 M_{\odot} \text{ yr}^{-1}$ over this (albeit larger) redshift range. Reddy et al. (2008) measure a steeper faint-end slope for the UV luminosity density at $z \sim 2$, $\alpha = -1.88$. If this behaviour is reflected in the general star-forming population at this redshift, we would also expect a steeper $H\alpha$ faint-end slope. This would increase the extrapolated ρ_{SFR} presented here. For example, fixing $\alpha = -1.65$ [more in line with the theoretical luminosity distribution from Bower et al. (2006), hereafter B06], ρ_{SFR} would increase by nearly a factor of 2. This should be taken as a cautionary point by the reader, when interpreting our extrapolated results.

There is a final caveat regarding the LF presented in Fig. 5; namely the treatment of dust. In this analysis, we have assumed a uniform correction, $A_{H\alpha} = 1$ mag, for ease of comparison with other results (we discuss the validity of this assumption in Section 4.2.2). Note that, in reality, this correction may be a function of luminosity, such that the most luminous systems require larger corrections. This

would have most effect on the bright end of the LF, where we suffer the most from low-number statistics.

4.1.3 Comparison to theoretical predictions of the luminosity distribution

Recent recipes for galaxy formation using a semi-analytic prescription provide us with the opportunity to directly compare observed $H\alpha$ line luminosities with theoretical predictions (B06). In Fig. 5, we present the $H\alpha$ LF at $z = 2.23$ from the B06 model which populates dark matter haloes in the N -body Milli-Millennium simulation with model galaxies (1/16 the volume of the full Millennium simulation; Springel et al. 2005). The B06 model is a variant of GALFORM, the Durham semi-analytic code (Cole et al. 2000; Benson et al. 2003), which includes a new prescription for AGN feedback. Such feedback appears to be very important for preventing the cooling of baryons in massive galaxies, and thus steepening the bright end of the LF (see B06). We take the *total* $H\alpha$ luminosity from the catalogue, and enforce the same equivalent width cut, $W_{H\alpha} > 50 \text{ \AA}$, as in our narrow-band selection. No other constraint is placed on other observable parameters. The observed luminosity distribution generally appears to agree well with the predictions, although there appears to be a slight excess of bright $H\alpha$ emitters in the model. The origin of this disparity could be caused by cosmic variance effects or overproduction of bright star-forming galaxies in the simulations, exacerbated by the low-number statistics in the high-luminosity bins. Nevertheless, the overall rough agreement of the $H\alpha$ luminosity density over the observed range is encouraging.

4.2 The properties of $H\alpha$ emitters

4.2.1 Hubble Space Telescope-Advanced Camera for Surveys imaging – morphologies

In Fig. 7, we present *Hubble Space Telescope*-Advanced Camera for Surveys (*HST*-ACS) F814W thumbnail images of the candidate $H\alpha$ emitters. The exquisite imaging from *HST* allows their rest-frame UV morphologies to be examined, and we have used this, along with *BRz* Subaru SuprimeCam optical imaging from the COSMOS archive, to preserve morphological information and reveal colour gradients that vary on scales comparable to ground-based imaging resolution. For example, this allows us to distinguish red and blue components in an interacting galaxy. We observe four morphological types: compact and isolated galaxies (33 ± 8 per cent); amorphous or disc morphologies (35 ± 8 per cent) and galaxies with obvious multiple components (27 ± 7 per cent). Note that several of the galaxies have too poor S/N in the *HST* images to determine a classification (5 ± 4 per cent). We note that the close-companion rate is only marginally above that for a similar K -band-selected sample: 21 per cent of $18 < K < 19.5$ galaxies selected from the full COSMOS survey have an $I < 25$ mag neighbour within 2.5 arcsec.

The mean half-light radius ($r_{1/2}$, an effective measure of galaxies' size) for the $H\alpha$ emitters is $\langle r_{1/2} \rangle = 2.1 \pm 0.5$ kpc. How do these galaxies compare with other UV-selected systems at the same epoch? Erb et al. (2004) report morphologies and sizes for 13 'BX' galaxies at $z \sim 2$ in the GOODS-N field (although these galaxies were selected partially for their known elongation, see also Förster-Schreiber et al. 2006). The 'BX' galaxies appear to have qualitatively similar properties to many of the $H\alpha$ -selected galaxies in this work: clumpy, 'tadpole' features (see also Law et al. 2007). BX galaxies in the Erb et al. (2004) sample have $r_{1/2} =$

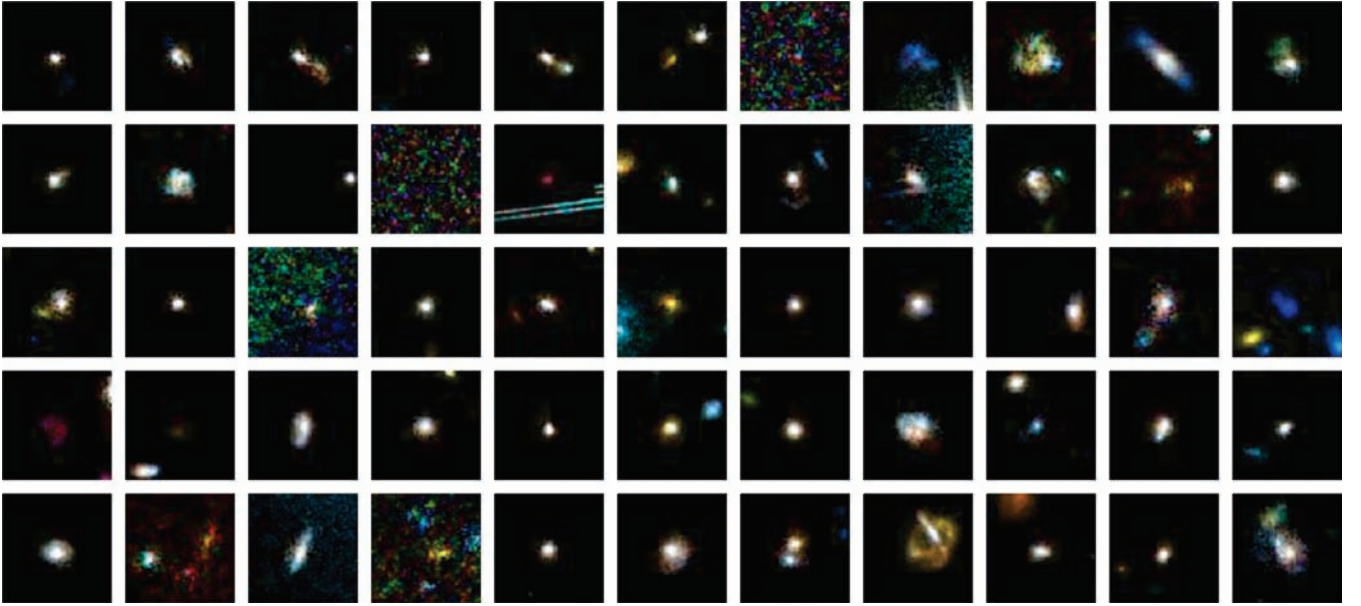


Figure 7. 5×5 arcsec² *HST*-ACS thumbnail images of the 55 $z = 2.23$ $H\alpha$ candidates. The images are coloured with a map generated from the ground-based *BRz* imaging, and use the F814W filter as a luminance channel (all images are scaled identically and orientated with north up and east to the left-hand side). Note that at $z = 2.23$, 5 arcsec is equivalent to ~ 40 kpc in projection. The images are organized row-wise in order of decreasing $H\alpha$ luminosity such that the top left thumbnail is the most luminous, and the bottom right is the least. There are two types of morphology: very compact or more extended (generally disturbed) systems. Many of the disturbed morphologies show evidence for two bright components within ~ 1 arcsec of each other – indicative of recent or ongoing interaction which might be powering star formation. The colour images appear to support this, with some of the more extended sources showing clear red and blue parts, reminiscent of merging star-forming galaxies in the local Universe.

1.9 ± 0.5 kpc, implying they have similar sizes (and qualitatively similar morphologies) to $H\alpha$ -selected star-forming galaxies at the same redshift.

4.2.2 *Spitzer* 24 μm and Very Large Array (VLA) 1.4 GHz observations – obscured star formation

The entire COSMOS field has been observed with the Multi-band Imaging Photometer (MIPS) on the *Spitzer Space Telescope*. The 24 μm flux at $z \sim 2.23$ probes polycyclic aromatic hydrocarbons (PAH) emission lines. In dusty star-forming galaxies at this redshift, 24 μm should be dominated by the prominent 7.7 μm emission feature, and so should be a good indicator of obscured star formation. To investigate the possibility that some of the $H\alpha$ emitters are dusty luminous starbursts, we cross-correlate the $H\alpha$ catalogue with the *Spitzer*-COSMOS (Sanders et al. 2006) MIPS 24 μm catalogues using a simple matching radius of 2 arcsec. Seven $H\alpha$ emitters from our sample of 55 are detected in both the wide and deep 24 μm MIPS maps (flux limits of 0.3 and 0.06 mJy, respectively) with a noise-weighted average 24 μm flux density of $\langle f_{24\mu\text{m}} \rangle = 0.20 \pm 0.03$ mJy.

In order to search for a statistical signature of mid-infrared emission from the whole sample of $H\alpha$ emitters, we stack the 24 μm data in regions around the source positions (the $H\alpha$ fluxes of 24 μm detections are not significantly different from the overall $H\alpha$ population, so we include these in the stack). The resulting stacked image yields a significant flux excess, $f_{24\mu\text{m}} = 0.11 \pm 0.01$ mJy. The uncertainty is derived by stacking 50×55 thumbnail images around random locations in the 24 μm map, and measuring the scatter in the fluxes measured in identical apertures in each stack. The significant 24 μm flux suggests weak mid-infrared emission in these star-forming galaxies. Since COSMOS was also observed at 70 and

160 μm with MIPS, we apply a similar stacking analysis for these wavelengths in an attempt to place constraints on the far-infrared properties of the $H\alpha$ emitters. We do not find significant flux excess in either case, and so we define 3σ upper limits of $f_{70\mu\text{m}} < 2.1$ mJy, and $f_{160\mu\text{m}} < 9.2$ mJy.

How does the infrared luminosity compare to the $H\alpha$ luminosity? To compare these two values, we first estimate the total-infrared luminosity by normalizing an M 82-like spectral energy distribution to the observed 24 μm flux and integrating over 8–1000 μm (the choice of SED is motivated by the discussion in Section 4.2.3). The SFR is estimated using the calibration of Kennicutt (1998), $\text{SFR}[\text{IR}] = 4.5 \times 10^{-45} (L_{8-1000\mu\text{m}}/\text{erg s}^{-1}) M_{\odot} \text{ yr}^{-1}$. We find $\text{SFR}[\text{IR}] = 90 \pm 40 M_{\odot} \text{ yr}^{-1}$, where the uncertainty is derived by recalculating the total infrared luminosity by introducing a 50 per cent variation in the normalization of the SED, since at $z = 2.23$ the 24 μm flux probes the 7.7 μm PAH emission line, and the fraction that this band can contribute to the total infrared flux can vary. How does this compare with the $H\alpha$ measurements? Without applying any correction for extinction at $H\alpha$, we calculate the average $\text{SFR}[H\alpha] = 40 \pm 20 M_{\odot} \text{ yr}^{-1}$ (the uncertainty reflecting the 1σ scatter in $H\alpha$ luminosities, and assuming $\text{SFR}[H\alpha] = 7.9 \times 10^{-42} (L_{H\alpha}/\text{erg s}^{-1}) M_{\odot} \text{ yr}^{-1}$; Kennicutt 1998). Including the canonical extinction correction of 1 mag, this rises to $\text{SFR}[H\alpha] = 100 \pm 45 M_{\odot} \text{ yr}^{-1}$ in good agreement with the SFR derived from the average infrared luminosity. As described above, the true level of extinction could be a function of luminosity, however this result suggests that our adoption of a constant reddening correction does not result in a significant underestimate of the SFR.

Four $H\alpha$ emitters are formally detected in the 1.4 GHz VLA map of COSMOS (Schinnerer et al. 2007), with an average flux of $\langle f_{1.4\text{GHz}} \rangle = 160 \pm 20 \mu\text{Jy}$. Again, these objects' $H\alpha$ fluxes are not significantly different from the general population, and so we

employ the same stacking technique to find the ‘average’ 1.4 GHz flux for the sample. We find $f_{1.4\text{GHz}} = 9.7 \pm 1.2 \mu\text{Jy}$ (the error is calculated in the same manner as the 24 μm stack – i.e. repeating the analysis for randomly co-added thumbnail images). Parametrizing the correlation between infrared and radio luminosity as $q_{24} = \log(f_{24\mu\text{m}}/f_{1.4\text{GHz}})$ (see Ibar et al. 2008), we find $q_{24} = 0.7 \pm 0.2$. This value is in good agreement with the expected q_{24} for an M82 SED at $z = 2.23$, $q_{24} = 0.6 \pm 0.1$ (Ibar et al. 2008), and so converting the radio luminosity to a far-infrared luminosity (and thus SFR) is consistent with our derived SFRs from the 24 μm luminosity and extinction-corrected $\text{H}\alpha$ luminosity described above.

4.2.3 Average spectral energy distribution of $\text{H}\alpha$ emitters

In Fig. 8, we show the average spectral energy distribution of the $\text{H}\alpha$ emitters. The optical/near-IR *uBVgrizK+F814W+IRAC 3.6–8 μm* photometry is averaged over all the $\text{H}\alpha$ emitters (weighted by the individual photometric errors) and then fitted with a choice of Sa-d and burst spectral templates (Bruzual & Charlot 1993) redshifted to $z = 2.23$ using the HYPERZ photometric redshift code (Bolzonella, Miralles & Pelló 2000). Note that the IRAC measurements are the 3 arcsec aperture fluxes corrected to total flux using the values suggested by the S-COSMOS team: 0.90, 0.90, 0.84 and 0.73 for the 3.6, 4.5, 5.8 and 8 μm cameras, respectively. Coverage of the rest-frame near-infrared is useful for improving the photometric redshifts of high-redshift objects since it allows the location of the 1.6 μm stellar bump to be tracked (e.g. Sawicki 2002). The wavelength of this feature corresponds to the minimum opacity of H^- ions in the atmospheres of cool stars (John 1988), and thus is an indicator of the evolved ($\gtrsim 20$ Myr old) stellar population. The

average 3.6–8 μm SED agrees with the 1.6 μm feature redshifted to $z = 2.23$. The data are well fitted by an Sc spectral-type template with a foreground screen reddening of $A_V = 1.0$ mag (this parameter was free to vary in the range $0 < A_V < 2$). This suggests the UV continuum in these sources may be slightly more obscured than we are assuming for the $\text{H}\alpha$ line emission.

The good fit to the spectral template is compelling evidence that our narrow-band plus photometric selection is indeed identifying a population of $z = 2.23$ star-forming galaxies, and shows that improved photometric redshifts that make use of bands redwards of K will help in improving the narrow-band selection (Mobasher et al. 2007). As IRAC is probing rest-frame near-infrared emission, we can estimate the stellar mass of these galaxies from the absolute rest-frame K -band luminosity. We estimate the rest-frame absolute K -band magnitude from the 5.8 μm flux, $M_K = -25.4$ mag (AB magnitude). The stellar mass, M_* , is estimated using a similar method to Borys et al. (2005), assuming M_* is equal to the integrated stellar mass at the age of the galaxy. Note that our template assumes a continuous star formation history, with a Miller & Scalo (1979) IMF (a burst template does not provide a satisfactory fit to the observed photometry). If the K -band luminosity traces stellar mass, then $M_* = 10^{-0.4(M_K - 3.3)} / (L_K/M) M_\odot$ where L_K/M is the mass-to-light ratio, and the factor of 3.3 corresponds to the absolute solar K -band luminosity (Cox 2000). For continuous star formation, we estimate L_K/M from the description of Borys et al. (2005) who use the STARBURST99 stellar synthesis code (Leitherer et al. 1999) to find $L_K/M = 103(\tau/\text{Myr})^{-0.48}$ for ages $\tau > 100$ Myr. The age returned from HYPERZ is 1 Gyr, similar to the mean age of $z \sim 2$ UV-selected star-forming galaxies in the survey of Erb et al. (2006). Adopting a realistic range in ages, 0.5–2 Gyr, we find $M_* \sim 6.1\text{--}11.5 \times 10^{10} M_\odot$. This is larger than the mean stellar mass of the sample in Erb et al. (2006), who find $M_* = (3.6 \pm 0.4) \times 10^{10} M_\odot$, but the disparity between the two mass estimates may be simply due to the different derivation methods used: comparison of the spectral energy distributions to stellar synthesis models in Erb et al. (2006) versus simple age-dependent mass-to-light ratios here.

In addition to the UV-near-IR photometry, we also show in Fig. 8 the longer wavelength data described above: 24 μm , 70 μm , 160 μm and 1.4 GHz cm statistical detections and limits. For comparison, we show the M82 galaxy SED (a local starburst) redshifted to $z = 2.23$ and scaled in flux to match the 24 μm flux density accordingly. The average 24 μm /1.4 GHz flux is consistent with what would be expected for a typical star-forming galaxy at $z = 2.23$ (Boyle et al. 2007; Ibar et al. 2008). This suggests that on average these galaxies are unremarkable starbursts, with SFRs $\lesssim 100 M_\odot \text{yr}^{-1}$, with properties broadly similar to the most actively star-forming galaxies found in the local Universe. We note, however, that there is a departure from the similarity to M82 in the rest-frame UV, with our composite SED showing quite significant UV excess over what would be expected from M82 at this redshift (Ibar et al. 2008). We interpret this as indicating that perhaps on average, the observed $\text{H}\alpha$ emitters are not as dusty as the local Luminous Infrared Galaxy (LIRG), or they simply have higher escape fractions of UV photons.

4.3 Clustering of $\text{H}\alpha$ emitters

4.3.1 Evaluating the clustering strength

Estimating the clustering properties of star-forming galaxies can be a powerful tool in understanding their formation and evolution because the clustering strength provides information about the dark matter haloes these galaxies reside in. The descendants (and progen-

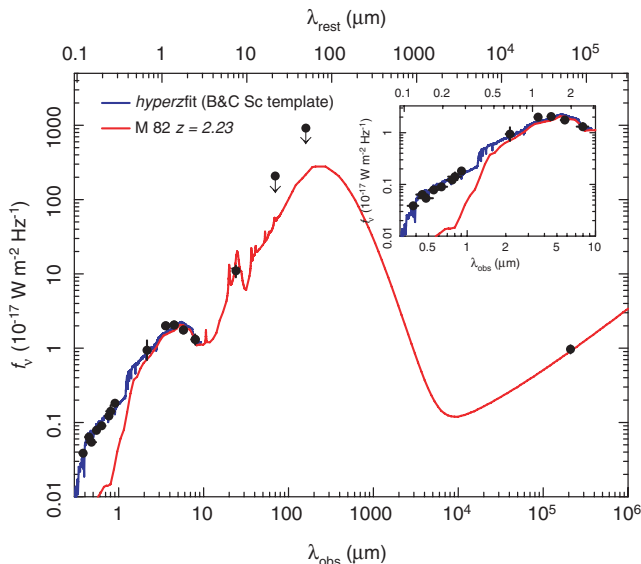


Figure 8. The average SED for $\text{H}\alpha$ emitters based on UV-radio photometry from the COSMOS archive averaged over all 55 candidates. In the inset, we fit these with a Sc galaxy template at $z = 2.23$ reddened by $A_V = 1$ mag. The fit agrees well with the average SED, suggesting that our narrow-band selection is indeed identifying star-forming galaxies at $z = 2.23$. The main panel extends the SED to longer wavelengths by stacking the 24 μm , 70 μm , 160 μm and 1.4 GHz data (the 70 and 160 μm points are 3σ upper-limits), and we overlay the M82 template, redshifted to $z = 2.23$ and scaled in flux accordingly. Again, this seems to verify the redshift selection and suggests that the galaxies we select are similar to local starburst galaxies in their broad SEDs.

itors) of these galaxies can then be traced by analysing the evolution of the haloes themselves. Despite our relatively small sample size, we note that it is selected in a relatively narrow redshift range with little dilution of the projected clustering, so we attempt to estimate the clustering strength of H α emitters using the angular correlation function, $\omega(\theta)$, from which we can derive the physical correlation length, r_0 . We use the estimator proposed by Landy & Szalay (1993):

$$\omega(\theta) = 1 + \left(\frac{N_R}{N_D}\right)^2 \frac{DD(\theta)}{RR(\theta)} - 2 \frac{N_R}{N_D} \frac{DR(\theta)}{RR(\theta)}. \quad (4)$$

Here, $DD(\theta)$ is the number of pairs of real ‘data’ galaxies within $(\theta, \theta + \delta\theta)$, $DR(\theta)$ is the number of data–random pairs and $RR(\theta)$ is the number of random–random pairs. N_R and N_D are the number of random and data galaxies in the survey. The random catalogue is generated by uniformly distributing $20N_D$ false galaxies over a geometry corresponding to the survey field-of-view, which is appropriate for the small sample. The errors for each angular interval (spaced at 0.25 dex) are estimated with $\delta\omega(\theta) = (1 + \omega(\theta))/\sqrt{DD(\theta)}$, which estimates the Poisson noise in each bin (Landy & Szalay 1993). We present our results in Fig. 9, and fit the data with a power law of the form $A\theta^{-0.8}$, where A is the amplitude of the angular correlation function, and the power-law index -0.8 is the fiducial value. For θ in

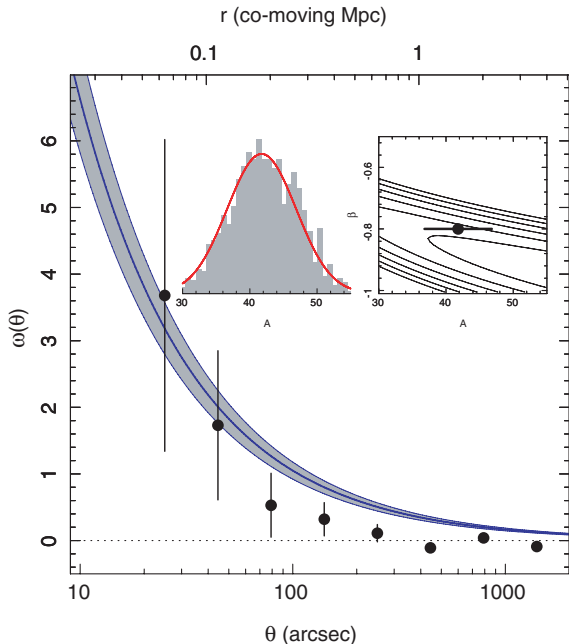


Figure 9. The two-point angular correlation function of H α emitters, $\omega(\theta)$. The data are fit with a power law $A\theta^{-0.8}$, and we find $A = 41.8 \pm 5.0$ (for θ in arcsec), corresponding to a correlation length $r_0 = 4.2^{+0.4}_{-0.2} h^{-1}$ Mpc. The insets show the likely uncertainty on the fit. The histogram shows the distribution of amplitudes when $\omega(\theta)$ is recalculated for a different realization of the random catalogue (this was repeated 1000 times). The contour plot represents χ^2 when the fit is allowed to vary both the amplitude and slope β of the power-law fit, thus demonstrating the covariance dependence on the uncertainty in A . We find an adequate fit is obtained without varying β , and therefore in our estimates we fix it at the fiducial value of $\beta = -0.8$, but it appears a better fit would be found for $\beta \sim -1$, and a larger amplitude. The effect of this increase in amplitude and β would correspond to a slight decrease in r_0 : $A = 95, \beta = -1$ corresponds to $r_0 \sim 3.6 h^{-1}$ Mpc; in better agreement with the measurement from the simulation (Section 4.3.2). Thus, our current estimate of the clustering strength might be a slight overestimate. These are preliminary findings – a better estimate requires a larger sample. However, these initial results suggest moderate clustering on scales of 10–100 arcsec (i.e. sub-Mpc or sub-halo).

arcsec, we find $A = 41.8 \pm 5.0$. The uncertainty is the 1σ range of A when the fit is repeated for 1000 realizations of $\omega(\theta)$, with different random catalogues. The integral constraint, C , which accounts for bias introduced by only observing a small region of the sky, will result in a reduction of the amplitude of the two-point correlation function: $A(\theta^{-0.8} - C)$. We estimate the effect following Roche et al. (2002), and find it to be small for our survey area, with $C = 0.0055$ for θ in arcsec – we include it when fitting the amplitude A .

A more useful description of the physical clustering of galaxies is the real-space correlation length, r_0 , and this can be calculated directly from the angular correlation function using the inverse Limber transformation (Peebles 1980; Efsthathiou et al. 1991) which relates the spatial correlation function to the angular correlation function (provided the redshift distribution is known).

Using clustering simulations described below, we have modelled the effect of the Gaussian filter selection function on our clustering measurements. We compare the projected clustering amplitude, A , derived for the population in a uniformly selected volume (i.e. assuming a top-hat transmission function) to that derived for samples selected with a luminosity-dependent selection function appropriate for our filter transmission curve. We find no statistical difference when including a luminosity-dependent volume correction, with $\langle A_{\text{Gaussian}} \rangle \simeq \langle A_{\text{uniform}} \rangle \sim 45$, using 100 simulations for each method. Therefore, for simplicity in the following deprojection analysis, we treat the projected correlation amplitude as if it came from a uniformly selected sample over the narrow redshift slice at $z = 2.22\text{--}2.25$. We also assume that the real-space correlation function is independent of redshift over this narrow range (this is the same approach used in other high-redshift narrow-band surveys; e.g. Kovač et al. 2007).

We find $r_0 = 4.2^{+0.4}_{-0.2} h^{-1}$ Mpc, where the uncertainty is derived by reevaluating r_0 after applying the 1σ uncertainty on the fit to $\omega(\theta)$ described above. This likely underestimates the true error due to added effects such as cosmic variance, which the reader should note could be an important effect in our $220 \times 10^3 \text{ Mpc}^3$ survey and to assess this we now turn to our simulations.

4.3.2 Comparison to theoretical predictions of the clustering properties of star-forming galaxies

In addition to the luminosity distribution predicted by semi-analytic recipes (Section 4.2.2), we can also compare observed clustering properties of H α emitters to theoretical predictions from these same models. The B06 model populates dark matter haloes within a Λ cold dark matter (Λ CDM) framework cosmology, where the ‘observable’ properties such as optical luminosity are dictated by a physically motivated prescription for the behaviour of baryons cooling within the haloes. Thus, we can directly evaluate r_0 for H α emitters within the simulation volume.

Taking the B06 model, we limit simulated luminosities to the range $42 \leq \log L_{\text{H}\alpha} (\text{erg s}^{-1}) \leq 44$ (approximately the range of observed luminosities) and $W_{\text{H}\alpha} > 50 \text{ \AA}$, and then project the positions of the galaxies on to a 2D ‘sky’. We then measure the amplitude of the two-point angular correlation function and convert to r_0 in exactly the same way as before (Section 4.3.1). We find $r_0 = 5.7^{+0.6}_{-0.7} h^{-1}$ Mpc, slightly larger than our observed value (but within $\sim 2\sigma$). Part of this disparity could be due to the slight excess of bright H α emitters in the simulations: the clustering of H α emitters in the $z = 0.24$ study of Shioya et al. (2008) was seen to increase with $L_{\text{H}\alpha}$. The reader should also take into account the relatively small size of our survey (despite it being the largest to date)

compared to the effective area of the Milli-Millennium. Thus, there are additional uncertainties on our estimate of r_0 due to the likely field-to-field variations which are still significant on this scale.

One way of illustrating this is to randomly select sub-volumes in the Milli-Millennium box corresponding to our survey volume. Projecting galaxies selected in these sub-volumes allows us to evaluate the amplitude of their angular correlation function in an identical way to that performed in Section 4.3.1. The scatter in amplitude (fixing the power-law slope to the fiducial value, -0.8 , as before) for a set of random positions is a good indicator of the expected cosmic variance on these scales. Statistically, we find a similar amplitude to the real data, $\langle A \rangle \sim 45 \pm 31$ (for θ in arcsec), but with large scatter from the field-to-field variations. Thus, the dominant source of uncertainty in our measurement of the clustering strength of these objects is cosmic variance, exacerbated by the relatively small numbers of objects in our sample.

4.3.3 Halo mass

The bias parameter describes how the observed galaxy distribution traces the underlying matter distribution. Assuming a model for the evolution of bias over cosmic time, it is possible to estimate the host halo mass of different galaxy populations by comparing their correlation length, r_0 , to that of galaxies within haloes of various mass. More importantly, this analysis can provide clues to determine the progenitor populations of galaxy populations in the local Universe. In Fig. 10, we compare our results to predictions

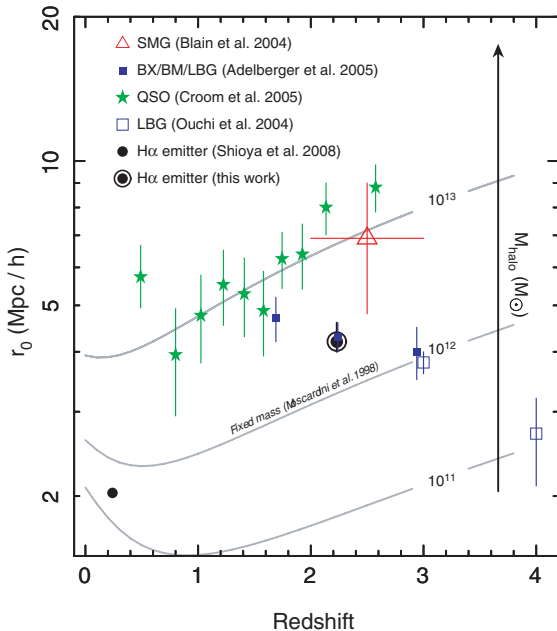


Figure 10. Evolution of the correlation length r_0 in comoving Mpc for a variety of galaxy populations over $z = 0-4$. Literature points include sub-mm galaxies (Blain et al. 2004); QSOs (Croom et al. 2005); LBGs (Ouchi et al. 2004, 2005); BM/BX galaxies (Adelberger et al. 2005) and local $H\alpha$ -selected galaxies (Shioya et al. 2008). We relate the clustering properties to the expected clustering from models of the clustering of dark matter haloes, assuming a model for the evolution of bias (Moscardini et al. 1998). Our results suggest that $H\alpha$ emitters at $z = 2.23$ are hosted by dark matter haloes of mass $\sim 10^{12} M_\odot$ – in good agreement with the masses of haloes expected to host similarly selected galaxies at the same redshift (i.e. BM/BX galaxies). Thus, these $H\alpha$ emitters appear to be the progenitors of Milky Way-like galaxies at $z = 0$.

of $r_0(z)$ for dark matter haloes with a fixed *minimum* mass dark matter haloes of mass $M_{\min} > 10^{11-13} h^{-1} M_\odot$ (Matarrese et al. 1997; Moscardini et al. 1998). This has become a popular way to present the results of clustering analyses in a cosmological context (e.g. Overzier et al. 2003; Blain et al. 2004; Farrah et al. 2006). We assume a Λ CDM cosmology, and an evolving bias model $b(z)$ (Moscardini et al. 1998). We use the values tabulated by Moscardini et al. (1998) for various fixed minimum mass haloes. We evaluate the predicted r_0 of galaxies by solving $\xi_{\text{gal}}(z) = D(z)^2 b(z)^2 \xi_{\text{DM}}(0)$, where $D(z)$ is the growth factor and ξ is the real-space correlation function.

Our results suggest that $H\alpha$ emitters at $z = 2.23$ reside in moderate-mass haloes, with M_{\min} of the order of $10^{12} M_\odot$, similar to that of a Milky Way mass halo at $z = 0$, suggesting that these high-redshift star-forming galaxies are the progenitors of M_* galaxies seen today. Given that the semi-analytic model is tied directly to the underlying dark matter haloes, it is possible to extract the halo masses that the B06 $H\alpha$ emitters actually reside in. Limiting the model luminosities to the observed range, we find halo masses spanning $\log M_{\text{halo}}(M_\odot) = 11.2-12.9$, with a median of $\log M_{\text{halo}}(M_\odot) = 11.7$. This is in reasonable agreement with the halo mass estimate from the observed deprojected angular correlation function.

In comparison to other active populations at the same epoch [QSOs, submillimetre galaxies (SMGs) and UV-selected BX/BM galaxies], we see that $H\alpha$ emitters typically reside in lower-mass haloes than SMGs and QSOs and are not directly related to them, but the $H\alpha$ emitters have a similar clustering strength to BX/BMs at the same redshift (Fig. 10). This is perhaps not surprising, given the overlap in selection between the two populations (Fig. 3), and suggests moderate clustering of star-forming galaxies at this redshift.

5 SUMMARY

We have presented results from the largest near-infrared narrow-band survey for $H\alpha$ emission at $z = 2.23$ yet undertaken, probing 220×10^3 comoving Mpc^3 to a $H\alpha$ line flux of $1 \times 10^{-16} \text{ erg s}^{-1} \text{ cm}^{-2}$. Selecting potential $z = 2.23$ $H\alpha$ emitters on the basis of the significance of their narrow-band excess at $2.121 \mu\text{m}$ and broad-band colours and magnitudes, we detect 55 galaxies over 0.603 deg^2 in the COSMOS field, a volume density of $(2.5 \pm 0.3) \times 10^{-4} \text{ Mpc}^{-3}$. Our findings can be summarized as follows.

(i) The LF is well fit by a Schechter function with $\phi^* = (1.45 \pm 0.47) \times 10^{-3} \text{ Mpc}^{-3}$, $\log L^* = 42.83 \pm 0.13 \text{ erg s}^{-1}$, assuming a faint-end slope of $\alpha = -1.35$, as found by Gallego et al. (1995) for the $H\alpha$ LF at $z = 0$. We find strong evolution in the $H\alpha$ LF from $z = 0$ to 2.23 equivalent to a $10\times$ increase in characteristic luminosity. The $z = 2.23$ LF is very similar to the $z = 1.3$ distribution of Yan et al. (1999), implying little evolution in the population between these epochs. We note, however, that deeper observations will be required to probe the faint end of the LF, which could impact our estimate of the integrated ρ_{SFR} .

(ii) The extinction-corrected SFRD determined from the integrated LF is $0.17^{+0.16}_{-0.09} M_\odot \text{ yr}^{-1} \text{ Mpc}^{-3}$ for $L_{H\alpha} > 10^{42} \text{ erg s}^{-1}$ $z = 2.23$ (including a 15 per cent correction for AGN contamination to the luminosity density). This result for the first time directly traces the evolution of ρ_{SFR} out to $z = 2.23$ using $H\alpha$ alone, and supports the view that the SFRD undergoes a plateau at $z \sim 1-2$ prior to sharp decline to the present day.

(iii) The $H\alpha$ emitters have infrared and radio properties similar to that expected for local star-forming galaxies: our statistical

measurement as of the 24 μm and 21 cm flux densities is consistent with a LIRG SED at $z = 2.23$, with the infrared-derived SFR agreeing with the H α derived rate if we assume the canonical H α extinction, $A_{\text{H}\alpha} = 1$ mag. However, in comparison to M 82 (an archetypal LIRG), we observe an UV light excess over the template, which suggests that these galaxies are not as obscured as M 82, or at least the escape efficiency of UV photons is higher in these galaxies. *HST*-ACS imaging reveals that the H α emitters have a range of morphologies including compact and disturbed systems: several comprise two components separated on scales of $\lesssim 10$ arcsec kpc, indicating recent or ongoing merger activity, as might be expected for starburst galaxies. Quantitatively, the rest-frame UV morphologies of the H α emitters are similar to UV-selected star-forming ('BX') galaxies at the same redshift, with mean half-light radii of $r_{1/2} = 2.1 \pm 0.5$ kpc.

(iv) We have performed the first clustering analysis of H α emitters at $z = 2.23$. First, we measure the amplitude of the two-point angular correlation function $\omega(\theta)$, and find $A = 41.8 \pm 5.0$ for θ in arcsec. The inverse Limber transform provides us with the real-space correlation length r_0 , which we find is $r_0 = 4.2_{-0.2}^{+0.4} h^{-1}$ Mpc. Comparing this result to other galaxy populations over cosmic time, these high-redshift star-forming galaxies have similar clustering properties to similarly selected galaxies at high and low redshift, and reside in dark matter haloes of masses of $\sim 10^{12} M_{\odot}$. This agrees with the range of masses of host haloes of H α emitters selected from the Millennium simulation. Our H α emitters appear to be slightly less strongly clustered than QSOs and SMGs, but similar to BX/BM galaxies at this redshift. Comparisons to models of clustering evolution taking into account bias evolution, our results suggest that these galaxies will likely evolve into L^* galaxies, similar to the Milky Way at $z = 0$.

These observations represent the first results of an innovative survey for emission-line objects over several square degrees at $z = 0.84$, 1.47 and 2.23 corresponding to narrow-bands in *J*, *H* and *K*: the Hi-Z Emission Line Survey (HiZELS) on UKIRT. The outcome of this survey will be large samples (~ 1000 at each redshift) of identically selected 'typical' star-forming galaxies within well-defined volumes. The large area will enable us to place even stronger constraints on the star formation history over this crucial epoch from identically selected star-forming galaxies in each redshift slice. Our custom-made *J* and *H* narrow-band filters at 1.204 and 1.618 μm , respectively, will not only detect H α emission at $z = 0.84$ and 1.47, but also detect [O II] $\lambda 3727$ and [O III] $\lambda 5007$ emission lines from sources at $z = 2.23$, exactly the same redshift as the current 2.121 μm survey. This will be a useful test for confirming the redshifts of a subset $z = 2.23$ H α emitters by matching to detections in these other narrow-band filters. It will also provide a more complete survey of the emission-line population of star-forming galaxies and AGN at this epoch.

ACKNOWLEDGMENTS

We thank the referee for a careful reading of the manuscript, and appreciate several helpful suggestions that have improved the quality of this work. JEG and KC thank the UK Science and Technology Research Facility (STFC; formerly PPARC) for financial support and IS and PNB acknowledge the Royal Society. JK thanks the German Science Foundation for financial support by way of SFB439. The authors wish to thank Calton Baugh, Richard Bower, Gavin Dalton, Helmut Dannerbauer, Alastair Edge, Vince Eke, Duncan Farrah, John Helly, Cedric Lacey, Simon Lilly, Bahram

Mobasher, Marco Riello, Tom Shanks and David Wake for helpful discussions. Finally, it is a pleasure to thank the support astronomers and telescope support staff at JAC/UKIRT who provided an excellent service throughout the observations required to complete this work: Andy Adamson, Luca Rizzi, Tom Kerr, Thor Wold, Tim Carroll and Jack Ehle. UKIRT is funded by the STFC.

REFERENCES

- Adelberger K. L., Steidel C. C., Shapley A. E., Hunt M. P., Erb D. K., Reddy N. A., Pettini M., 2004, *ApJ*, 607, 226
 Adelberger K. L., Steidel C. C., Pettini M., Shapley A. E., Reddy N. A., Erb D. K., 2005, *ApJ*, 619, 697
 Aragón-Salamanca A., Alonso-Herrero A., Gallego J., García-Dabó C. E., Pérez-González P. G., Zamorano J., Gil de Paz A., 2003, in Perez E., Gonzalez Delgado R. M., Tenorio-Tagle G., eds, *ASP Conf. Ser. Vol. 297, Star Formation Through Time*. Astron. Soc. Pac., San Francisco, p. 191
 Avni Y., Soltan A., Tananbaum H., Zamorani G., 1980, *ApJ*, 238, 800
 Beckwith S. V. W., Thompson D., Mannucci F., Djorgovski S. G., 1998, *ApJ*, 504, 107
 Benson A. J., Bower R. G., Frenk C. S., Lacey C. G., Baugh C. M., Cole S., 2003, *ApJ*, 599, 38
 Bertin E., Arnouts S., 1996, *A&AS*, 117, 393
 Blain A. W., Chapman S. C., Smail I., Ivison R., 2004, *ApJ*, 611, 725
 Bolzonella M., Miralles J.-M., Pelló R., 2000, *A&A*, 363, 476
 Borys C., Smail I., Chapman S. C., Blain A. W., Alexander D. M., Ivison R. J., 2005, *ApJ*, 635, 853
 Bower R. G., Benson A. J., Malbon R., Helly J. C., Frenk C. S., Baugh C. M., Cole S., Lacey C. G., 2006, *MNRAS*, 370, 645 (B06)
 Boyle B. J., Terlevich R. J., 1998, *MNRAS*, 293 L49
 Boyle B. J., Shanks T., Croom S. M., Smith R. J., Miller L., Loaring N., Heymans C., 2000, *MNRAS*, 317, 1014
 Boyle B. J., Cornwell T. J., Middelberg E., Norris R. P., Appleton P. N., Smail I., 2007, *MNRAS*, 376, 1182
 Bruzual A. G., Charlot S., 1993, *ApJ*, 405, 538
 Bunker A. J., Warren S. J., Hewett P. C., Clements D. L., 1995, *MNRAS*, 273, 513
 Capak P. et al., 2007, *ApJS*, 172, 99
 Casali M. et al., B., 2007, *A&A*, 467, 777
 Chapman S. C., Blain A. W., Smail I., Ivison R. J., 2005, *ApJ*, 622, 772
 Cole S., Lacey C. G., Baugh C. M., Frenk C. S., 2000, *MNRAS*, 319, 168
 Cox A. N., 2000, in Cox A. N. ed., *Allen's Astrophysical Quantities*, 4th edn. Springer, New York
 Croom S. M. et al., 2005, *MNRAS*, 356, 415
 Cutri R. M. et al., 2003, 2MASS All Sky Catalogue of Point Sources, The IRSA 2MASS All-Sky Point Source Catalogue, NASA/IPAC Infrared Science Archive, Available at <http://irsa.ipac.caltech.edu/applications/Gator/>
 Daddi E., Cimatti A., Renzini A., Fontana A., Mignoli M., Pozzetti L., Tozzi P., Zamorani G., 2004, *ApJ*, 617, 746
 Dye S. et al., 2006, *MNRAS*, 372, 1227
 Erb D. K., Steidel C. C., Shapley A. E., Pettini M., Adelberger K. L., 2004, *ApJ*, 612, 122
 Erb D. K., Steidel C. C., Shapley A. E., Pettini M., Reddy N. A., Adelberger K. L., 2006, *ApJ*, 646, 107
 Efstathiou G., Bernstein G., Tyson J. A., Katz N., Guhathakurta P., 1991, *ApJ*, 380, L47
 Farrah D. et al., 2006, *ApJ*, 641, L17
 Förster-Schreiber N. et al., 2006, *ApJ*, 645, 1062
 Fujita S. S. et al., 2003, *ApJ*, 586, L115
 Gallego J., Zamorano J., Aragón-Salamanca A., Rego M., 1995, *ApJ*, 455, L1
 Glazebrook K., Blake C., Economou F., Lilly S., Colless M., 1999, *MNRAS*, 306, 843
 Hao L. et al., 2005, *AJ*, 129, 1795
 Hopkins A. M., 2004, *ApJ*, 615, 209

- Hopkins A. M., Connolly A. J., Haarsma D. B., Cram L. E., 2001, *AJ*, 122, 288
- Ibar E. et al., 2008, *MNRAS*, 386, 953
- Jansen R. A., Franx M., Fabricant D., 2001, *ApJ*, 551, 825
- John T. L., 1988, *A&A*, 193, 189
- Jones H. D., Bland-Hawthorn J., 2001, *ApJ*, 550, 593
- Kennicutt R. C. Jr, 1992, *ApJ*, 388, 310
- Kennicutt R. C. Jr, 1998, *ARA&A*, 36, 189
- Kennicutt R. C. Jr, Kent S. M., 1983, *AJ*, 88, 1094
- Kovač K., Somerville R. S., Rhoads J. E., Malhotra S., Wang J., 2007, *ApJ*, 668, 15
- Kurk J. D., Pentericci L., Overzier R. A., Röttgering H. J. A., Miley G. K., 2004, *A&A*, 428, 817
- Landy S. D., Szalay A. S., 1993, *ApJ*, 412, 64
- Law D. R. et al., 2007, *ApJ*, 656, 1
- Le Delliou M., Lacey C., Baugh C. M., Guiderdoni B., Bacon R., Courtois H., Sousbie T., Morris S. L., 2005, *MNRAS*, 357, L11
- Leitherer C. et al., 1999, *ApJS*, 123, 3
- Lilly S. J., Tresse L., Hammer F., Crampton D., Le Fevre O., 1995, *ApJ*, 455, 108
- Lilly S. J. et al., 2007, *ApJS*, 172, 70
- Ly C. et al., 2007, *ApJ*, 657, L738
- Madau P., Ferguson H. C., Dickinson M. E., Giavalisco M., Steidel C. C., Fruchter A., 1996, *MNRAS*, 283, 1388
- Matarrese S., Coles P., Lucchin F., Moscardini L., 1997, *MNRAS*, 286, 115
- Miller G. E., Scalo J. M., 1979, *ApJS*, 41, 513
- Mobasher B. et al., 2007, *ApJS*, 172, 117
- Moorwood A. F. M., van der Werf P. P., Cuby J. G., Oliva E., 2000, *A&A*, 326, 9
- Moorwood A., van der Werf P., Cuby J. G., Oliva T., 2003, in Bender R., Renzini A., eds, *Proc. ESO Workshop, The Mass of Galaxies at Low, High Redshift*. Springer-Verlag, Berlin, p. 302
- Moscardini L., Coles P., Lucchin F., Matarrese S., 1998, *MNRAS*, 299, 95
- Ouchi M. et al., 2004, *ApJ*, 611, 685
- Overzier R. A., Röttgering H. J. A., Rengelink R. B., Wilman R. J., 2003, *A&A*, 405, 53
- Pascual S., Villar V., Gallego J., Zamorano J., Pelló R., Díaz C., Aragón-Salamanca A., 2005, in Hidalgo-Gómez A. M., González J. J., Rodríguez Espinosa J. M., Torres-Peimbert S., eds, *Rev. Mex. Astron. Astrofis. Ser. Conf. Vol. 24, II International GTC Workshop: Science with GTC 1st-light Instruments and the LMT*. UNAM, Mexico, p. 268
- Peebles P. J. E., 1980, *The Large-Scale Structure of the Universe*. Princeton Univ. Press, Princeton, NJ
- Reddy N. A. et al., 2008, *ApJ*, 175, 48
- Roche N. D., Almaini O. D. J., Ivison R. J., Willott C. J., 2002, *MNRAS*, 337, 1282
- Sanders D. B. et al., 2006, *BAAS*, 38, 1211
- Sawicki M., 2002, *AJ*, 124, 3050
- Schinnerer E. et al., 2007, *ApJS*, 172, 46
- Scoville N. et al., 2007, *ApJS*, 172, 1
- Shaver P. A., Wall J. V., Kellermann K. I., Jackson C. A., Hawkins M. R. S., 1996, *Nat*, 384, 439
- Shioya Y. et al., 2008, *ApJS*, 175, 128
- Smail I., Ivison R. J., Blain A. W., Kneib J.-P., 2002, *MNRAS*, 331, 495
- Springel V. et al., 2005, *Nat*, 435, 629
- Steidel C. C., Giavalisco M., Pettini M., Dickinson M., Adelberger K. L., 1996, *ApJ*, 462, L17
- Steidel C. C., Adelberger K. L., Shapley A. E., Pettini M., Dickinson M., Giavalisco M., 2003, *ApJ*, 592, 728
- Teplitz H. I., Malkan M., McLean I. S., 1998, *ApJ*, 506, 519
- Thompson D., Mannucci F., Beckwith S. V. W., 1996, *AJ*, 112, 1794
- Tresse L., Maddox S. J., Le Fèvre O., Cuby J.-G., 2002, *MNRAS*, 337, 369
- van der Werf P. P., Moorwood A. F. M., Bremer M. N., 2000, *A&A*, 362, 509
- Villar V. et al., 2008, *ApJ*, 677, 169
- Yan L., McCarthy P. J., Freudling W., Teplitz H. I., Malumuth E. M., Weymann R. J., Malkan M. A., 1999, *ApJ*, 519, L47

This paper has been typeset from a $\text{\TeX}/\text{\LaTeX}$ file prepared by the author.